

Article

Development of Membrane Electrode Assembly with Double-Catalytic Layer for Micro Direct Methanol Fuel Cell

Shubin Zhang¹ and Yanfeng Jiang^{1,2,*} 

¹ School of Internet of Things Engineering, Jiangnan University, Wuxi 214122, China; shubinzhang@jiangnan.edu.cn

² Institute of Advanced Technology, Jiangnan University, Wuxi 214122, China

* Correspondence: jiangyf@jiangnan.edu.cn

Abstract: This paper presents a membrane electrode assembly (MEA) with a double-catalytic layered structure to improve the performance of the micro direct methanol fuel cell. The inner and outer parts of the double-catalytic layer comprise an unsupported and carbon-supported catalyst, respectively. A two-dimensional two-phase model of mass transport and electrochemical reaction is established and simulated to analyze the superiority of the double-catalytic layered structure. Simulation results show that this structure has a more uniform current density distribution and less over-potential across the catalyst layer. Methanol crossover is also reduced. Experimental results confirm that the MEA with the double-catalytic layered structure exhibits better performance than the traditional MEA. The adoption of a gas diffusion electrode as the outer catalytic layer and a catalyst-coated membrane as the inner layer of the double-catalytic layered structure can further improve the performance of the MEA. Both simulation and experimental results show the existence of an optimum number of metal loadings of the inner and outer parts of the double-catalytic layer.

Keywords: direct methanol fuel cell; membrane electrode assembly; double-catalytic layer; gas diffusion electrode; catalyst coated membrane



Citation: Zhang, S.; Jiang, Y.

Development of Membrane Electrode Assembly with Double-Catalytic Layer for Micro Direct Methanol Fuel Cell. *Inventions* **2024**, *9*, 19. <https://doi.org/10.3390/inventions9010019>

Academic Editor: Shaik Gouse Peera

Received: 20 December 2023

Revised: 17 January 2024

Accepted: 19 January 2024

Published: 1 February 2024



Copyright: © 2024 by the authors. Licensee MDPI, Basel, Switzerland. This article is an open access article distributed under the terms and conditions of the Creative Commons Attribution (CC BY) license (<https://creativecommons.org/licenses/by/4.0/>).

1. Introduction

Given the rapid development of portable electric devices, the demand for micro power sources with high energy density has increased. The next generation of portable electric equipment requires significantly higher energy storage. However, a further increase in energy density is difficult to achieve for traditional batteries, such as Li-based batteries. Thus, fuel cells, which are highly suitable for applications that require extremely high energy density, have been receiving a great deal of attention because of their prospective energy density, technological feasibility, safety, and cost [1]. Among the various types of fuel cell, the direct methanol fuel cell (DMFC), which provides power by converting the chemical energy of methanol and oxygen into electrical energy, is an attractive choice because of its significant advantages, including higher power density, instant recharging via methanol injection, lower weight compared with conventional batteries, and simpler and more compact structure [2–5]. Manufacturers (Ultracell, MTI Micro, Toshiba, Hitachi, Fujitsu, and Samsung, among others) in a number of countries have realized the promising application of DMFCs, and several prototypes have been developed.

As a key component of the DMFC, the membrane electrode assembly (MEA), which is the site of the electrochemical reactions, has a layered structure, including an anode/cathode diffusion layer, anode/cathode catalyst layer, and proton exchange membrane. The fuel passes the gas diffusion layer and takes part in the electrochemical reaction in the catalyst layer. Thus, the structure of the catalyst layer can significantly affect cell performance. To construct a functioning and stable catalyst layer, the most important thing is to develop high-performance catalysts. Recently, Pt-free or even metal-free catalysts for

DMFCs have attracted a lot of attention. The aim is to use earth-abundant materials as catalysts to make the fuel cell more cost-effective and environmentally friendly. However, research thus far has been in the form of laboratory experiments, which have not yet been successfully implemented for applicable real-world fuel cell devices [6–8]. Pt catalysts are still the most common and stable catalysts used in DMFCs, and they have been application-proofed [9]. Pt catalyst sites create a high density of atomic steps, edges, and kinks, which can break chemical bonds. The design of new supports for Pt catalysts has also been an alternative strategy to enhance catalyst stability and reduce the cost [10,11]. Kim et al. used carbon nanotubes, ammonium carbonate, and ammonium hydrocarbonate as pore-forming materials in the cathode catalyst layer to improve mass transport. The results showed that the power density increased by 30% to 40% because of the improved porosity [12,13]. By adding Vulcan XC-72R, Ketjen Black EC 300J, and Black Pearls 2000 carbon blacks to the cathode catalyst layer of Pt black, Wang et al. were able to more than double the power density of the prepared MEA [14,15]. Most efforts were put into tuning micropore structure and improving electrical conductivity through use of carbon materials [10,16–18]. In these ways, the reactive surface area of the catalysts and their electrochemical activity are improved, while Ohmic loss is reduced to as little as possible. In addition, the catalyst layer structure is also crucial to fuel cell performance. Studies show that metal loadings and MEA thickness have an optimal value which relates to the trade-offs among mass transport efficiency, ion conductivity, and true active surface area [19–21]. Therefore, the structural design of the catalyst layer should be considered when fabricating an MEA.

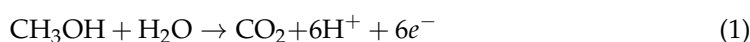
MEA performance is also affected by the way that the catalyst layer is fabricated, and significant research efforts have been exerted in investigating novel fabrication procedures [22–27]. Tsai et al. placed Pt-Ru nanoparticles in dense carbon nanotubes that directly grow on carbon cloth, and this method decreased the Pt-Ru load to 0.4 mg cm^{-2} and increased the power density by 27% [23]. Tang et al. adopted a decal transfer method to produce a catalyst layer [27]. The catalyst was first coated onto the Nafion membrane to form a catalyst-coated membrane (CCM) and was then sandwiched between gas diffusion layers through hot pressing. The fabricated MEA decreased methanol crossover by 55% and increased the power density by 36%.

In this work, a novel MEA with a double-catalytic layered structure, within which both the CCM method and the traditional method were used, was fabricated to show improved performance. The superiority of the double-catalytic layered structure was investigated through establishing a two-dimensional (2D) two-phase model and adopting a finite element method. Furthermore, thorough experimental tests validated the numerical results.

2. Materials and Methods

2.1. Mathematical

A 2D two-phase model is presented to describe mass transport and the electrochemical reaction inside the double-catalytic layered MEA under isothermal steady-state conditions. Nine sub domains are shown in Figure 1a, and an enlarged view of the MEA is shown in Figure 1b. Furthermore, the complete structure of the double-catalytic layered MEA comprises seven layers: an anode gas diffusion layer (AGDL), an outer anode catalyst layer (OACL), an inner anode catalyst layer (IACL), a polymer electrolyte membrane (PEM), an inner cathode catalyst layer (ICCL), an outer cathode catalyst layer (OCCL), and a cathode gas diffusion layer (CGDL). The outer catalyst layers are carbon supported, whereas the inner catalyst layers are not. The reactions take place in the ACL and CCL. On the anode, methanol and water react to form carbon dioxide and generate protons and electronics, as described in Equation (1). Meanwhile, oxygen on the cathode reacts with protons and electronics to form water, as shown in Equation (2).



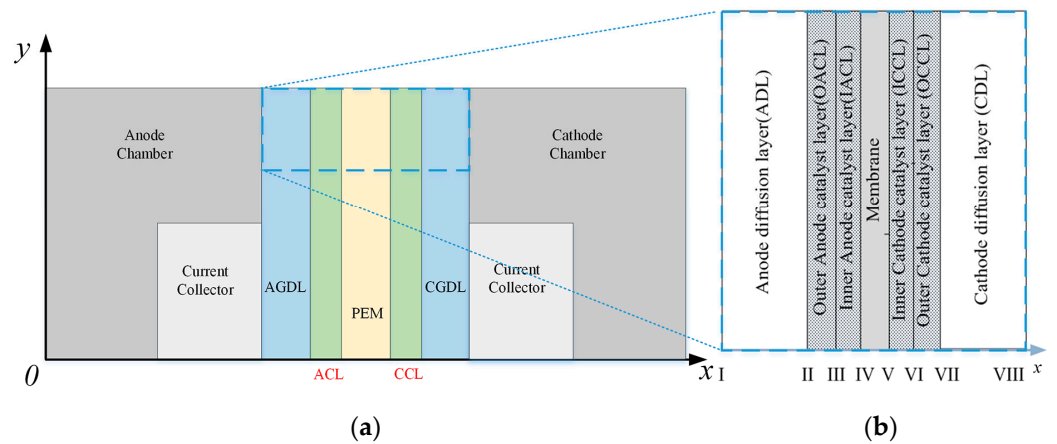


Figure 1. (a) Schematic of the simulation domains of the MEA. (b) Enlarged view of the double-catalytic structure.

For convenience of description, the principles of mass and momentum transportations in porous regions are first presented, and the electrochemical kinetics and the current balance are then formulated to complement the model. Boundary conditions at the interfaces I to VIII are included in the model, and the MEA geometric dimensions, operating conditions, and physicochemical properties are presented in Table 1.

Table 1. Operating parameters and physicochemical properties.

Parameters	Symbols	Value	Unit	Ref.	
Thickness Porosity Permeability	ADL	$\delta_{ADL}, \varepsilon_{ADL}, K_{ADL}$	$2 \times 10^{-4}, 0.7, 1 \times 10^{-12}$	m, -, m ²	[28]
	OACL	$\delta_{OACL}, \varepsilon_{OACL}, K_{OACL}$	$2 \times 10^{-5}, 0.3, 2 \times 10^{-14}$	m, -, m ²	[28]
	IACL	$\delta_{IACL}, \varepsilon_{IACL}, K_{IACL}$	$1 \times 10^{-5}, 0.1, 2 \times 10^{-14}$	m, -, m ²	[28]
	MEM	$\delta_{MEM}, -, K_{MEM}$	$1.8 \times 10^{-4}, -, 2 \times 10^{-18}$	m, -, m ²	[28]
	ICCL	$\delta_{ICCL}, \varepsilon_{ICCL}, K_{ICCL}$	$0.1 \times 10^{-4}, 0.1, 2 \times 10^{-14}$	m, -, m ²	[28]
	OCCL	$\delta_{OCCL}, \varepsilon_{OCCL}, K_{OCCL}$	$0.2 \times 10^{-4}, 0.3, 2 \times 10^{-14}$	m, -, m ²	[28]
Diffusivities	CDL	$\delta_{CDL}, \varepsilon_{CDL}, K_{CDL}$	$2 \times 10^{-4}, 0.7, 1 \times 10^{-12}$	m, -, m ²	[28]
		D_m	$1.58 \times 10^{-9} e^{0.02623(T-298)}$	m ² s ⁻¹	[28]
		D_{O_2}	$1.78 \times 10^{-5} (T/273)^{1.823}$	m ² s ⁻¹	[28]
		$D_{m,mem}$	$4.9 \times 10^{-10} e^{[2463(1/333-1/T)]}$	m ² s ⁻¹	[28]
Operating temperature	T	298	K	-	
Anode inlet pressure	p_1^{in}	1.01×10^5	Pa	-	
Cathode inlet pressure	p_g^{in}	1.01×10^5	Pa	-	
Inlet methanol concentration	$C_{m,in}$	2.0	M	-	
Inlet oxygen concentration	$C_{O_2,in}$	9.35×10^{-3}	M	-	
Viscosity of gas phase	μ_g	2.03×10^{-5}	kg m ⁻¹ s ⁻¹	[28]	
Viscosity of liquid phase	μ_l	4.05×10^{-4}	kg m ⁻¹ s ⁻¹	[28]	
Electro-osmotic drag coefficients of water and methanol	n_{d,H_2O}	$2.9e^{[1029(1/333-1/T)]}$	-	[29]	
	$n_{d,m}$	$n_{d,H_2O} x_m$	-	[28]	
Proton conductivity in membrane and catalyst layers	κ_m	$7.3e^{[1268(1/298-1/T)]}$	S m ⁻¹	[28]	
	κ_c	0.1416	S m ⁻¹	[30]	
Thermodynamic potential	E_0	1.21	V	[28]	
Transfer coefficient of anode and cathode	α_a	0.5	-	[28]	
	α_c	1.0	-	[28]	

Table 1. Cont.

Parameters	Symbols	Value	Unit	Ref.
Anode exchange current density in OACL and IACL	$A_{v,a,OACL/m}^{ref}$ $A_{v,a,IACL/m}^{ref}$	1.0×10^5 1.5×10^5	$A m^{-3}$ $A m^{-3}$	[28] -
Cathode exchange current density in ICCL and OCCL	$A_{v,c,ICCL/O_2}^{ref}$ $A_{v,c,OCCL/O_2}^{ref}$	6.97×10^2 1.05×10^3	$A m^{-3}$ $A m^{-3}$	[28] -
Anode reference concentration	C_m^{ref}	0.1	M	[28]
cathode reference concentration	$C_{O_2}^{ref}$	3.65×10^{-2}	M	[28]
Surface tension	σ	0.0644	$N m^{-1}$	[28]
Contact resistance	$R_{contact}$	8×10^{-5}	Ωm^2	[28]

The AGDL and the catalyst layers on the anode are all porous regions. The methanol solution transfers from the AGDL to the catalyst layers, where the methanol oxidation reaction (MOR) occurs, and carbon dioxide is formed. Meanwhile, the produced carbon dioxide transfers from the IACL to the AGDL, simultaneous with the transportation of methanol. Thus, a two-phase flow must be modeled.

The mass transportation of methanol in porous regions is governed by the convection-diffusion equation:

$$\nabla \cdot (-D_m^{eff} \nabla C_m) + \mathbf{u}_1 \cdot \nabla C_m = R_m \tag{3}$$

where D_m^{eff} , C_m , \mathbf{u}_1 , and R_m denote the effective diffusion coefficient, concentration, liquid phase flow velocity vector, and the mole generation rate of methanol, respectively.

The liquid flow velocity vector \mathbf{u}_1 can be obtained from the momentum transport equation, known as Darcy’s law:

$$\mathbf{u}_1 = -\frac{Kk_{rl}}{\mu_1} \nabla p_1 \tag{4}$$

where K donates the absolute permeability of the porous medium, μ_1 is the dynamic viscosity of the liquid-phase, and k_{rl} stands for the relative permeability of a liquid phase as related to the liquid saturation. In a porous medium, the gas phase shares the space with the liquid phase, reducing the effective motion space and affecting the velocity of the liquid phase. k_{rl} is the correction coefficient of liquid phase velocity, shown as:

$$k_{rl} = s^3 \tag{5}$$

where s represents the liquid saturation in a porous medium. The effective diffusion coefficient of methanol in a porous region is given as:

$$D_m^{eff} = D_m \varepsilon^{1.5} (1 - s)^{1.5} \tag{6}$$

where D_m represents the absolute diffusivity of methanol, and ε is the porosity.

The driving force for the produced carbon dioxide to move outwards is the pressure difference between the gas and liquid phases, which arises from the surface tension and is also called capillary pressure:

$$p_c = p_g - p_l = \sigma \cos(\theta_c) \left(\frac{\varepsilon}{K}\right)^{0.5} J(s) \tag{7}$$

where P_g donates the pressure of the gas phase, P_l is the pressure of the liquid phase, σ represents the surface tension coefficient, θ_c is the contact angle, ε is the porosity of the porous media and $J(s)$, the Leverette function, is expressed as follows:

$$J(s) = \begin{cases} 1.417(1 - s) - 2.120(1 - s)^2 + 1.263(1 - s)^3 & 0 < \theta_c < 90^\circ \\ 1.417s - 2.120s^2 + 1.263s^3 & 90^\circ < \theta_c < 180^\circ \end{cases} \tag{8}$$

Analogously with the liquid phase, the governing equations for the gas phase are written as:

$$\mathbf{u}_g = -\frac{Kk_{rg}}{\mu_g} \nabla p_g \quad (9)$$

$$\nabla \left(\frac{\rho_g}{M_{CO_2}} \mathbf{u}_g \right) = R_{CO_2} \quad (10)$$

where M_{CO_2} and R_{CO_2} represent the molar mass and the mole generation rate of carbon dioxide, respectively. k_{rg} is the relative permeability of the gas phase:

$$k_{rg} = (1 - s)^3 \quad (11)$$

In the following, the governing equations of the cathode are given in a simple way because the two-phase condition on the cathode is very similar to that on the anode. The mass transport of the gas phase on the cathode is described as:

$$\nabla \cdot (-D_{O_2}^{eff} \nabla C_{O_2}) + \mathbf{u}_g \cdot \nabla C_{O_2} = R_{O_2} \quad (12)$$

where μ_g denotes the velocity of the mixed gases of N_2 , O_2 , and water vapor, which can be obtained using the Maxwell–Stefan equation:

$$\mathbf{n}_i = \left\{ -\rho_g w_i \sum_{j=1}^3 \frac{MD_{ij}}{M_j} (\nabla w_j + \frac{w_j}{M} \nabla M) + w_i \rho_g \mathbf{u}_g \right\} \quad (13)$$

where \mathbf{n}_i stands for the mass flux of component i , ρ_g is the mixed gas density, w_i is defined as the mass fraction of species i , M and M_j are the molar masses of the mixture and species j , and D_{ij} describes the diffusion coefficient of species i in component j .

Darcy's law for momentum transport of the liquid phase has the same formulation as Equation (2). The velocity is decided by:

$$\nabla \left(\frac{\rho_l}{M_{H_2O}} \mathbf{u}_l \right) = R_{H_2O} - R_w \quad (14)$$

Note that R_{H_2O} stands for the mole generation rate of water produced by the ORR, and R_w represents the interfacial transfer rate of water between the liquid and vapor phases. Here R_w is set to be zero, which means that water transfer between the liquid and gas phases is neglected. This simplification has little effect on the relevance of the following discussion.

On interface I, the methanol concentration is set as constant:

$$C_m = C_{m,in} \quad (15)$$

On interface III, the liquid saturation is assumed to be:

$$s = 0.95 \quad (16)$$

The boundary condition for oxygen on interface VIII:

$$C_{O_2} = C_{O_2,in} \quad (17)$$

The gas phase pressure and the liquid saturation on interface VIII are:

$$p_g = p_{atm} \quad (18)$$

$$s = 0.05 \quad (19)$$

On the anode, the simplified Tafel-like expression is used for the MOR kinetics:

$$j_a = A_{v,a} j_m^{\text{ref}} \left(\frac{C_m}{C_m^{\text{ref}}} \right)^\gamma \exp\left(\frac{\alpha_a F}{RT} \eta_a\right) \quad (20)$$

where $A_{v,a}$ is the specific area, C_m is the methanol concentration, C_m^{ref} and j_m^{ref} stand for the reference methanol concentration and transfer current density, α_a is the anode transfer coefficient, and η_a represents the anode overpotential. The reaction order γ is related to the methanol concentration and is assumed to be zero when methanol concentration is higher than the reference value. Otherwise, a first-order reaction is specified:

$$\gamma = \begin{cases} 1 & C_m < C_m^{\text{ref}} \\ 0 & C_m \geq C_m^{\text{ref}} \end{cases} \quad (21)$$

The anode overpotential η_a is defined as:

$$\eta_a = \phi_s - \phi_m - E_{\text{eq}}^a \quad (22)$$

where ϕ_s and ϕ_m stand for the potentials of the electronic phase and the electrolyte at the reaction site, respectively. E_{eq}^a is the thermodynamic open circuit potential of the anode at the operational temperature. Based on this, the mole generation rate of methanol, R_m , is finally obtained as follows:

$$R_m = -\frac{j_a}{6F} \quad (23)$$

Similarly, the rate of ORR, which takes place on the cathode, is governed by:

$$j_c = A_{v,c} j_{\text{O}_2}^{\text{ref}} \left(\frac{C_{\text{O}_2}}{C_{\text{O}_2}^{\text{ref}}} \right)^\gamma \exp\left(-\frac{\alpha_c F}{RT} \eta_c\right) \quad (24)$$

The cathode overpotential is defined as:

$$\eta_c = \phi_s - \phi_m - E_{\text{eq}}^c \quad (25)$$

Thus, the mole generation rate of oxygen can be obtained from:

$$R_{\text{O}_2} = -\frac{j_c}{4F} \quad (26)$$

To describe the potential distribution in the seven subdomains, the following equations are used:

$$\nabla(-\kappa_s \nabla \phi_s) = 0, \text{ in ADL and CDL} \quad (27)$$

$$\nabla(-\kappa_m \nabla \phi_m) = 0, \text{ in MEM} \quad (28)$$

$$\nabla(-\kappa_s \nabla \phi_s) = -j_a, \nabla(-\kappa_m \nabla \phi_m) = j_a, \text{ in ACLs} \quad (29)$$

$$\nabla(-\kappa_s \nabla \phi_s) = j_c, \nabla(-\kappa_m \nabla \phi_m) = -j_c, \text{ in CCLs} \quad (30)$$

The cell current is measured through the protons and electrons produced by the MOR in the anode catalyst layers:

$$I_{\text{Cell}} = \int_{\text{ACLs}} j_a dx \quad (31)$$

Methanol crossover is a serious issue for DMFC and causes a heavy loss in cell voltage. To account for the effect of methanol crossover, it is assumed that the methanol permeated from the anode is completely oxidized on the cathode. Thus, a ‘‘parasitic’’ current density is calculated as:

$$I_p = 6F \cdot N_{\text{cross}} \quad (32)$$

where F is Faraday's constant, and N_{cross} stands for the mole flux of methanol permeated from the anode, depending mainly on the effect of electro-osmotic drag and molecular diffusion. Thus, the flux of methanol crossover can be determined as:

$$N_{\text{cross}} = n_{\text{d,m}} \cdot \frac{I_{\text{Cell}}}{F} - D_{\text{m,mem}} \nabla C_{\text{m}} \quad (33)$$

On the cathode, the current density generated by the ORR is:

$$I_{\text{c}} = \int_{\text{CCLs}} j_{\text{c}} dx \quad (34)$$

The relationship among the cathode current, the "parasitic" current, and the cell current is:

$$I_{\text{c}} = I_{\text{p}} + I_{\text{Cell}} \quad (35)$$

Finally, the cell voltage can be determined as:

$$E_{\text{Cell}} = E_0 - \eta_{\text{a}} + \eta_{\text{c}} - I_{\text{Cell}} \left(R_{\text{contact}} + \frac{\kappa_{\text{m}}}{\delta_{\text{mem}}} \right) \quad (36)$$

where E_0 , R_{contact} and κ_{m} denote the cell's thermodynamic equilibrium voltage, the contact resistance, and the membrane's proton conductivity, respectively.

2.2. Experimental

The fabrication methods for the catalysts and PEM, as well as the pretreatment for Nafion membranes, are as follows. These can also be found elsewhere in the literature [19].

A slurry containing XC-72, PTFE (20 wt.%), and Nafion (10 wt.%) was coated onto carbon paper (TGPH060, 10 wt.% PTFE) to prepare the GDL. Carbon-supported catalysts, 40 wt.% Pt-20 wt.% Ru/C and 40 wt.% Pt/C, purchased from Johnson Matthey, Inc., were used for the fabrication of anode and cathode catalyst layers, respectively. Catalyst ink was prepared by dispersing an appropriate amount of catalyst and Nafion solution (Dupont, 5 wt.%) into a mixture of isopropyl alcohol and deionized (DI) water with a volume ratio of 1:1, and it was then sprayed onto the GDL to produce the gas diffusion electrode (GDE). Ionomer loading was 15 wt.% for the cathode or anode.

Commercial Nafion 117 membranes were treated by subsequently boiling at 80 °C for 2 h each in 2% H₂O₂, DI water, 1 M H₂SO₄, DI water, and 0.5 M NaOH. In this step, Pt-Ru black (with an atomic ratio 1:1) and Pt black (Johnson Matthey, Inc.) were respectively adopted as the anode and cathode catalysts with the same ionomer loading of 20 wt.%. Catalyst ink was uniformly sprayed onto Teflon decal blank, and it was then transferred to the Na⁺-Nafion 117 membrane by hot pressing at 160–200 °C and 5–9 MPa for 150 s to produce catalyst coated membrane (CCM). After that, the CCMs were ion-exchanged to the protonated form by boiling subsequently in 0.5 M H₂SO₄ and DI water at 80 °C each for 1 h.

The anode and cathode GDEs were attached to the CCM or Nafion 117 by hot-pressing at 135 °C and 10 MPa for 180 s to form a membrane electrode assembly (MEA) that has a working area of 1 cm². The MEA was sandwiched between two graphite plates with serpentine channel flow fields. A 2 M methanol solution was fed into the anode at a flow rate of 2 mL min⁻¹, and oxygen was fed into the cathode with the pressure kept at 2 atm. After experiencing an activation process, current–voltage (I – V) polarization curves were obtained at room temperature and the power density was determined from these I – V curves.

3. Results

The simulation results presented in this section are achieved by solving the above governing equations, and a finite element method aided by the software COMSOL Multiphysics 5.4 is adopted to perform the simulation.

Figure 2 shows the distribution of the anode current density in three different kinds of catalyst layer at a relatively high cell current density of 100 mA cm^{-2} . Interestingly, the current density in the unsupported catalyst layer decreases sharply from the AGDL/OACL interface to the IACL/PEM interface, whereas only slight declines are observed in both the double-catalytic layer and the supported catalyst layer, which vary in the opposite direction. The distribution of the current density in the double-catalytic layer is also found to be more uniform than that in the supported catalyst layer, indicating that the performance of the MEA with the former structure is better.

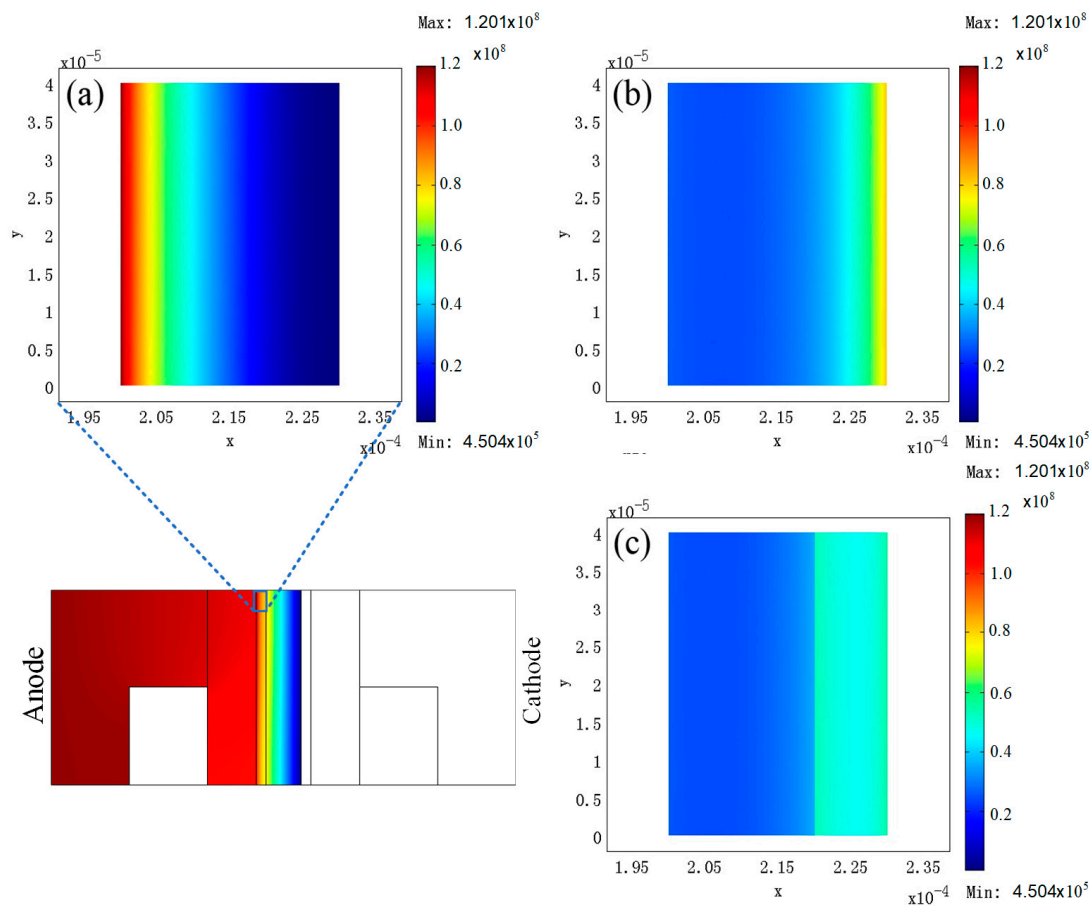


Figure 2. Anode current density in catalyst layers (A m^{-2}): (a) unsupported catalyst layer (b) carbon supported catalyst layer (c) double-catalytic layer.

The distributions of the methanol concentration and the anode over-potential are illustrated in Figures 3 and 4, respectively, to explain the variation in current density. The methanol concentration in the unsupported catalyst layer suffers a heavy drop from the AGDL/OACL interface to the IACL/PEM interface, facilitating a decrease in the anode current density in the same direction. One of the disadvantages of the unsupported catalyst layer is that concentration polarization forms easily, resulting in seriously limited fuel cell performance. Therefore, the double-catalytic layer exhibits worse distribution of methanol concentration than the carbon-supported catalyst layer, as shown in Figure 3.

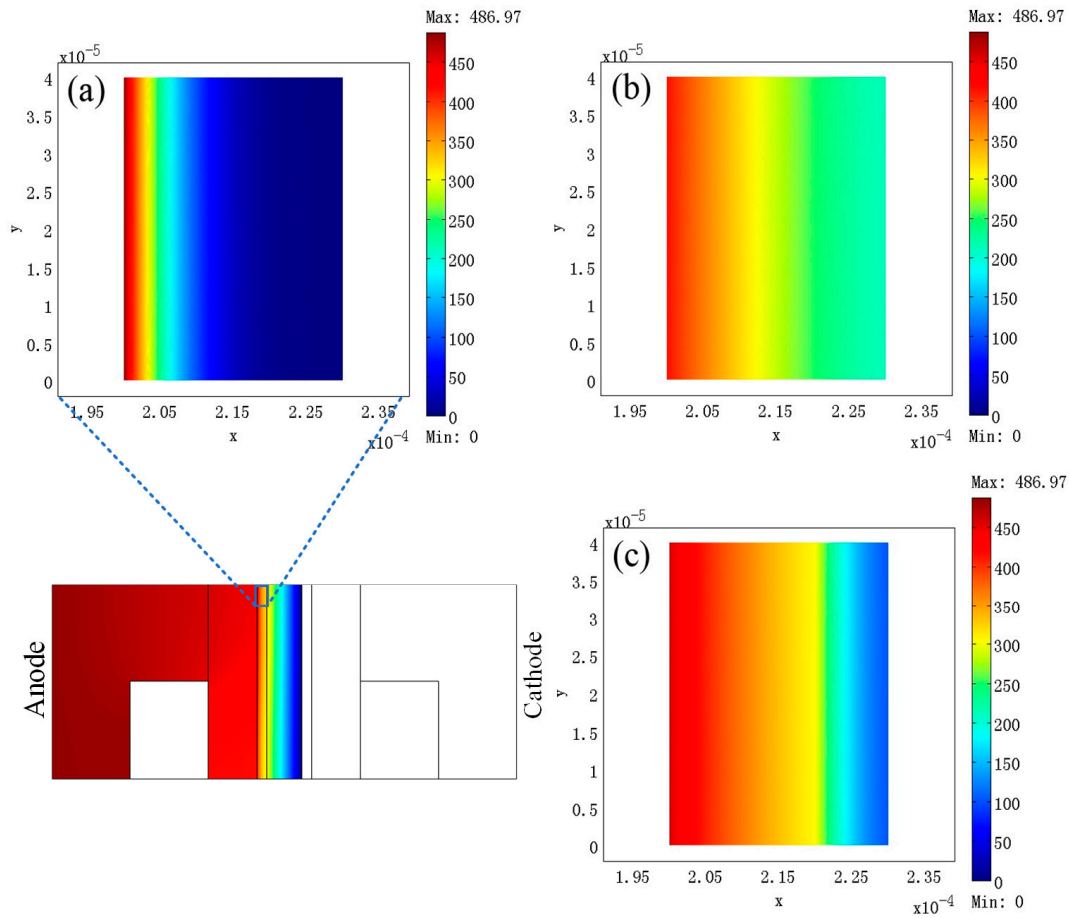


Figure 3. Methanol concentration in the catalyst layers (mol m^{-3}): (a) unsupported catalyst layer, (b) carbon supported catalyst layer, (c) double-catalytic layer.

In Figure 4, the anode over-potential across the unsupported catalyst layer is the highest among the three kinds of catalyst layers; as expected, the unsupported catalyst layer outputs the lowest cell voltage and the worst cell performance. Figure 4 also shows that the anode current density distributions of the double-catalytic layer and the carbon supported catalyst layer both follow the distribution of the anode over-potential. The anode over-potential across the double-catalytic layer is lower than that across the carbon-supported catalyst layer; that is, the double-catalytic layer has better electrochemical activity than the carbon-supported catalyst layer, which allows the double-catalytic layer to provide a higher cell voltage.

Figure 5 shows the distribution of the oxygen concentration in the cathode catalyst layer. Generally, the oxygen concentration decrease across the cathode catalyst layer is significantly smaller than the methanol concentration decrease across the anode catalyst layer. Consequently, the transport resistance of oxygen is significantly smaller than that of methanol because of the substantially larger diffusion coefficient of oxygen. However, the concentration decrease in the unsupported catalyst layer, 0.011 mol L^{-1} , is still the largest among that of the three layers. The other two values are 0.005 and 0.003 mol L^{-1} for the double-catalytic and supported catalyst layers, respectively.

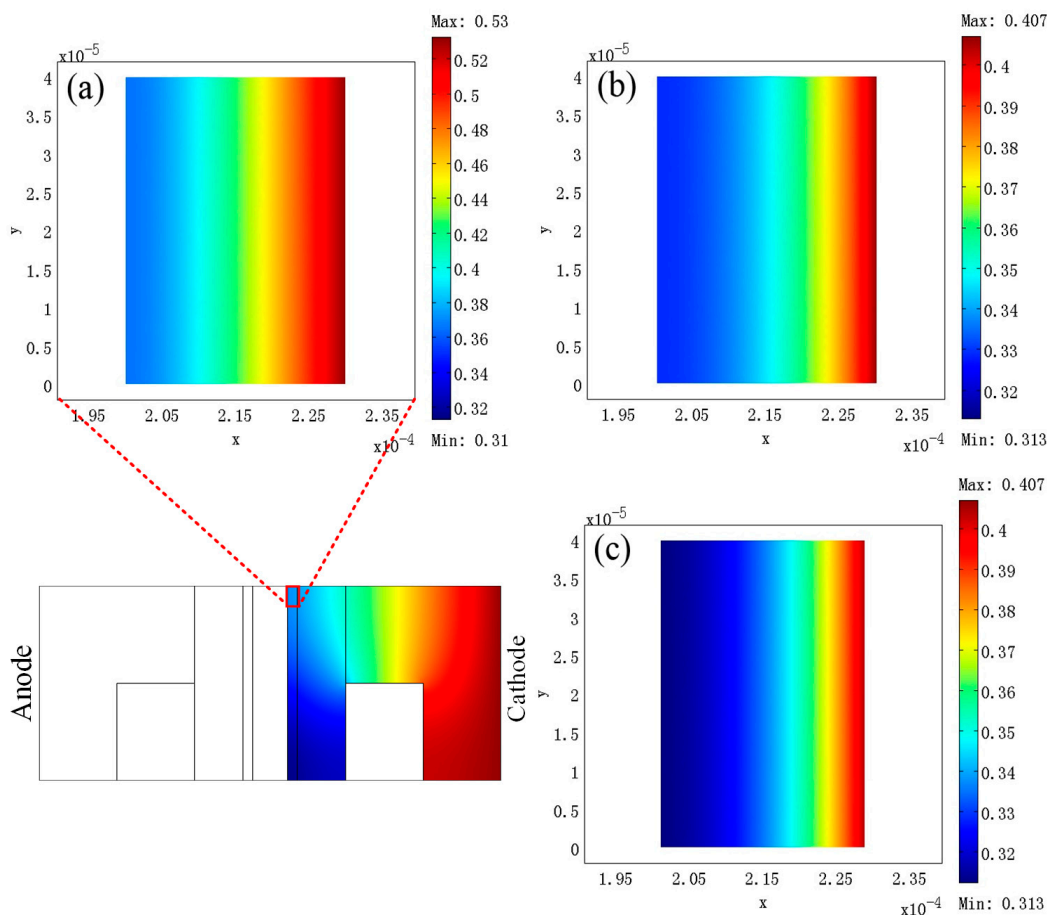


Figure 4. Anode over-potential in the catalyst layers (V): (a) unsupported catalyst layer, (b) carbon supported catalyst layer, (c) double-catalytic layer.

The distribution of the current density or over-potential on the cathode varies with the catalyst layer structure in the same way as the distribution on the anode does. Thus, these simulation results are not presented. The most serious problem on the cathode is methanol crossover, which varies with the discharge current density and catalyst layer structure, as shown in Figure 6. The flux of the methanol crossover in the unsupported catalyst layer is the smallest at any discharge cell current density, but this condition is a consequence of concentration polarization, and the cost is a significant decrease in cell performance. Compared with the double-catalytic layer, the supported catalyst layer suffers from a rather high methanol crossover, which directly increases the “parasitic” current. In the long term, this parasitic current reduces the fuel efficiency and energy density of the whole cell. Figure 6 also indicates that the methanol crossover decreases with increasing current density, which has been shown in another report [31]. The methanol crossover is primarily dependent on diffusion and electro-osmosis, both of which rely strongly on the methanol concentration at the IACL/PEM interface. The increasing current density results in a decrease in the methanol concentration in the IACL, and both the diffusion and electro-osmosis rates decrease accordingly. As a result, increasing current density results in a decrease in the methanol crossover.

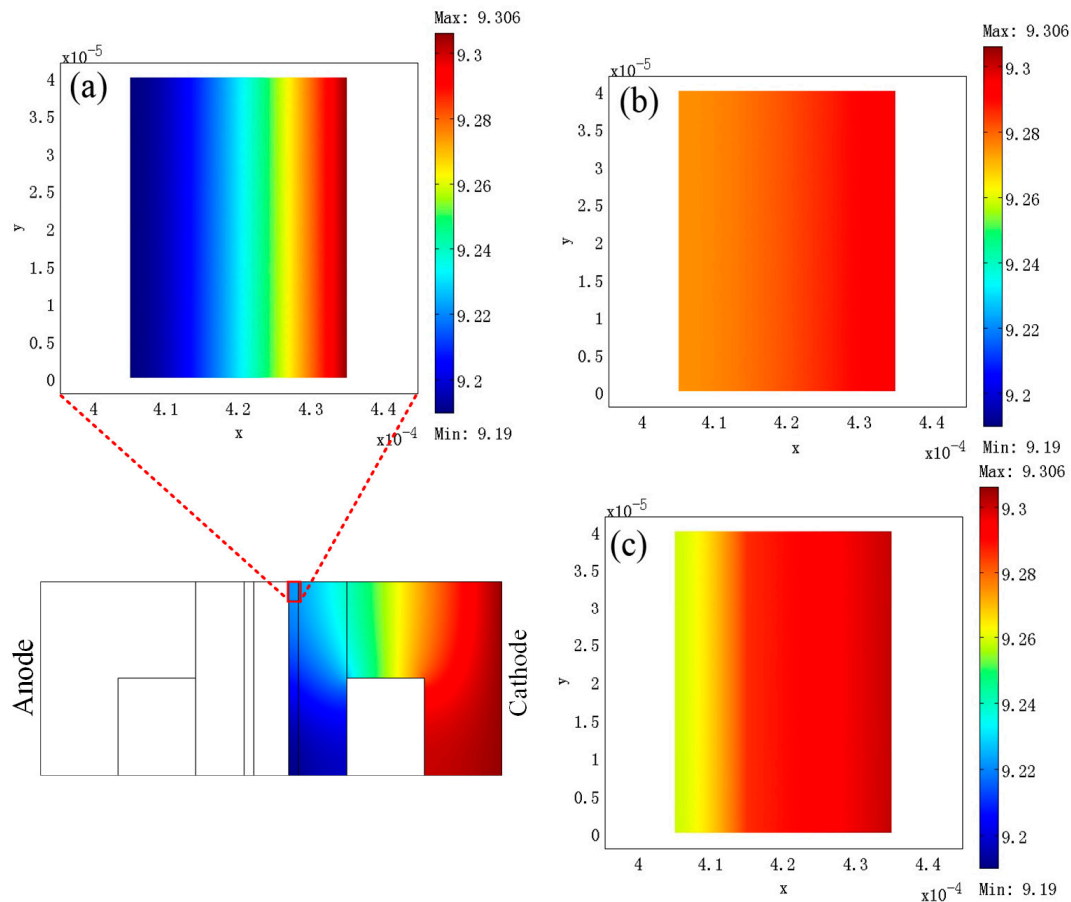


Figure 5. Oxygen concentration in the catalyst layers (mol m^{-3}): (a) unsupported catalyst layer, (b) carbon supported catalyst layer, (c) double-catalytic layer.

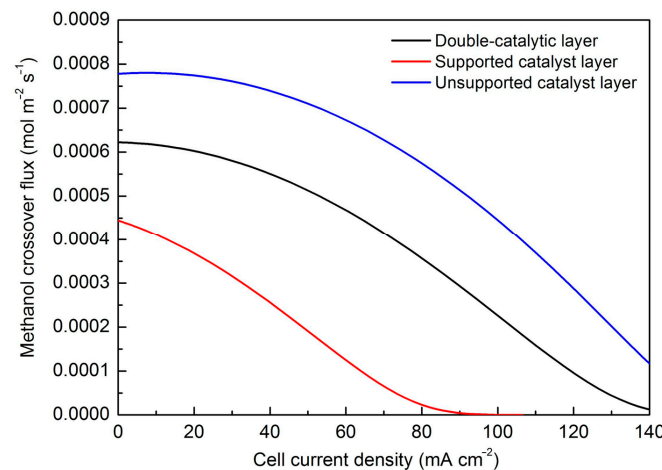


Figure 6. Simulation results of methanol crossover flux of different catalyst layers.

Figure 7 shows the simulated performance of DMFCs with different catalyst layers. Generally, the cell with the double-catalytic layer shows the best performance. However, some details should still receive close attention. At low discharge current densities, concentration polarization is negligible, and the unsupported catalyst layer provides the largest electrochemical active areas and the lowest methanol crossover, allowing it to exhibit the best performance. Given the increase in discharge current density, the unsupported catalyst layer undergoes serious concentration polarization, which significantly decreases performance. The double-catalytic layer effectively combines the advantages of unsupported and

carbon-supported catalysts, allowing the DMFC with a double-catalytic layered structure to achieve excellent performance.

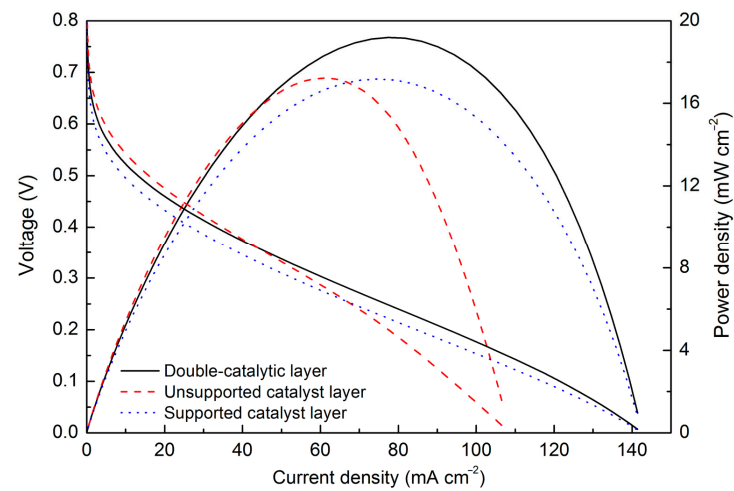


Figure 7. Simulation results of the performance of DMFCs with different catalyst layers.

4. Discussion

Figure 8 shows the performance of the micro DMFC prepared with different catalyst layer structures. With metal loadings of 4 mg cm^{-2} on the anode and 2 mg cm^{-2} on the cathode, the metal loadings of the inner and outer parts of the double-catalytic layer are set as equal. The cell prepared with a carbon-supported catalyst presents a higher peak power density (ca. 19.6 mW cm^{-2}) than that of the cell prepared with an unsupported catalyst (ca. 18.8 mW cm^{-2}) because of improved mass transportation. Compared with the supported catalyst layer, the double-catalytic layer exhibits larger mass transportation resistance, but it has more uniform current density distribution, smaller over-potential, and less methanol crossover, which make the cell with the double-catalytic layer output the highest peak power density of $\sim 23.6 \text{ mW cm}^{-2}$.

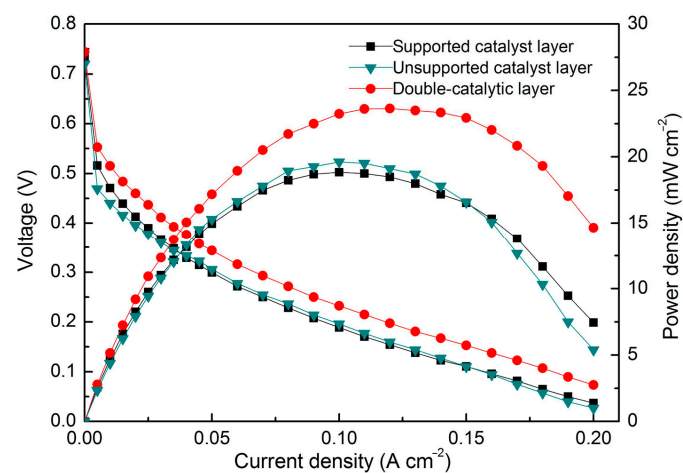


Figure 8. Performance of micro DMFCs fabricated with different catalyst layers.

Figure 9 shows the effects of fabrication method of the double-catalytic layer on the performance of the micro DMFC. The first MEA was prepared using the GDE method, that is, subsequently spraying the supported and unsupported catalysts onto the gas diffusion layer and then hot-pressing with Nafion 117. The second MEA was prepared using the CCM method, that is, subsequently coating the supported and unsupported catalysts onto Nafion 117 and then hot-pressing with anode and cathode gas diffusion layers. The last

MEA was prepared using a mixed GDE–CCM method, wherein the outer catalyst layer is GDE, and the inner layer is CCM. The metal loading of the inner catalyst layers equals that of the outer catalyst layers for the three MEAs, with a total metal loading of 4 mg cm^{-2} on the anode and 2 mg cm^{-2} on the cathode. Figure 9 shows that the MEA prepared using the GDE–CCM method has the highest peak power density among the three layers because this MEA possesses the advantages of both the GDE and CCM methods. The inner catalyst layer, prepared using the CCM method, has good contact with the Nafion membrane, which is beneficial in decreasing protonic and electronic resistance. The outer catalyst layer, prepared using the GDE method, has a large active surface area, and its three-dimensional porous structure can further increase the electrochemical surface area. Thus, the MEA prepared using the CCM–GDE method exhibits a significantly improved performance.

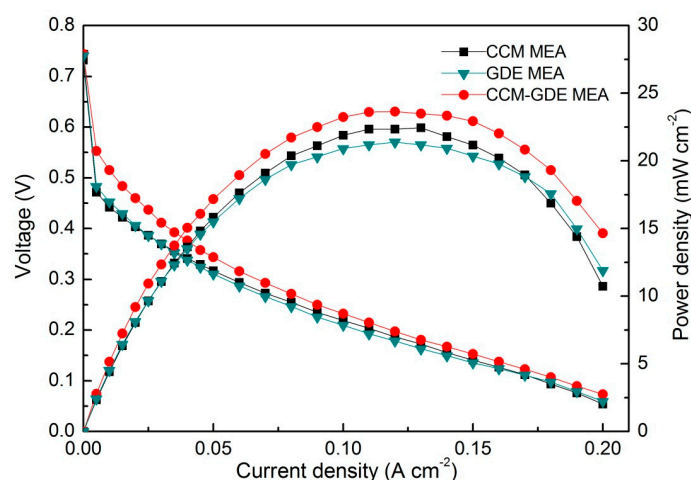


Figure 9. Performance of micro DMFCs fabricated with different procedures.

To optimize the structure of the double-catalytic layer, MEAs with different metal loading ratios between the outer and inner catalyst layers were fabricated and tested, and the results are shown in Figure 10. In Figure 10a, where the metal loadings of both the cathode outer and inner catalyst layers are 1.0 mg cm^{-2} , the highest peak power density of approximate 25.1 mW cm^{-2} is achieved when the metal loadings of the anode outer and inner catalyst layers are 2.5 and 1.5 mg cm^{-2} , respectively. In Figure 10b, where the metal loadings of the anode outer and inner catalyst layers are 2.5 and 1.5 mg cm^{-2} , respectively, the best performance is obtained when the metal loading of the cathode outer catalyst layer equals to that of the cathode inner catalyst layer. This is because exceedingly high metal loading of the inner catalyst layer is not beneficial in the improvement of mass transport, but too-small metal loading of the inner catalyst layer causes the electrochemical active area to decrease near the Nafion membrane. Thus, the metal loading ratio between the inner and outer catalyst layers should be set well to balance mass transportation and electrochemical activity.

The performance of the DMFC is compared with the ones reported in the literature, as listed in Table 2. With a power density of 25.1 mW cm^{-2} , the proposed MEA exhibits a competitive performance. The noble metal loadings of this MEA are kept at an extremely low level among these works. Here, we can obtain a normalized power density of the DMFC with noble metal loadings. It can be calculated as the power density divided by metal loadings. Thus, the novel design of the double-catalytic MEA structure has demonstrated a promising application prospect.

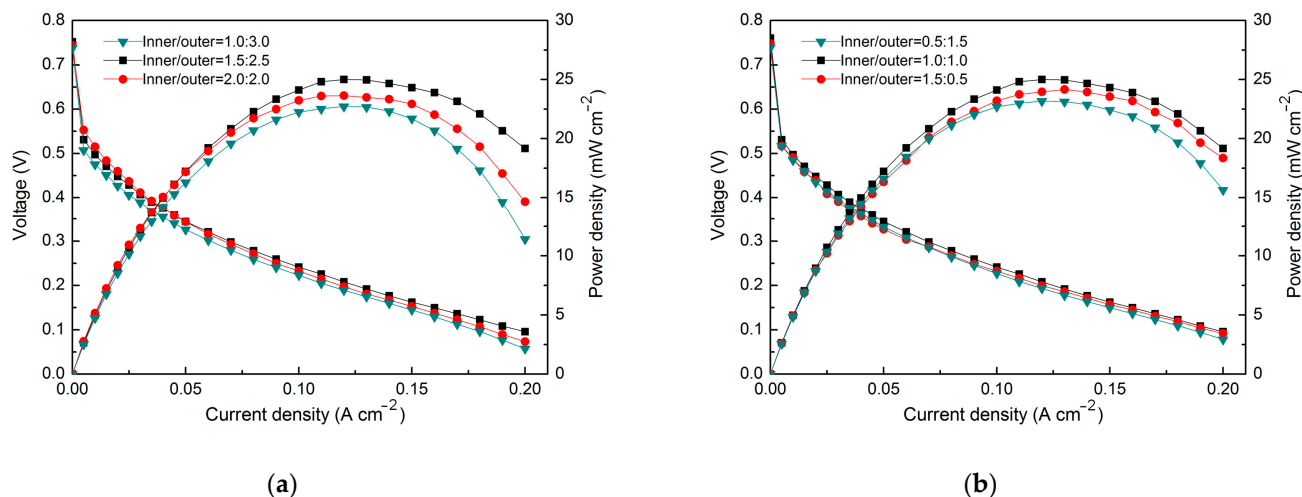


Figure 10. Performance of micro DMFCs fabricated with different metal loading ratios between the inner and outer catalyst layers of the (a) anode, and (b) cathode.

Table 2. Performance comparison with other DMFC catalyst layer designs in the literature.

Ref.	Catalyst Layer Design	Temperature (°C)	Power Density (mW cm ⁻²)	Total Noble Metal Loadings (mg cm ⁻²)
This work	Double-catalytic layer		25.1	
	Non-supported Pt	25	19.6	2.4
	Pt/C		18.8	
[16]	Pt/C	60	82.28	3.2
[19]	Pt/C	25	22.3	2.4
[32]	Pt-CeMoO/C	60	69.4	3.2
[33]	Pt/C	25	17.2	3
[34]	Pt/Polypyrrole nanowire	25	34.3	5

5. Conclusions

A membrane electrode assembly for a micro DMFC was designed with a double-catalytic layered structure, the inner and outer parts of which comprised unsupported and carbon-supported catalysts, respectively. Mathematical simulation results showed that the double-catalytic layered structure effectively combines the advantages of supported and unsupported catalysts. Although the double-catalytic layer has slightly larger mass transportation resistance than the carbon-supported catalyst layer, it produces significantly better electrochemical activity, characterized by a more uniform current density distribution and less over-potential across the catalyst layer. Moreover, the methanol crossover of the double-catalytic layer is also reduced. All of these factors result in an improvement in cell performance, which is also confirmed by the experimental results. Using a gas diffusion electrode as the outer catalyst layer and a catalyst-coated membrane as the inner catalyst layer, the fabricated DMFC can achieve a peak power density of 25.1 mW cm⁻². Using fixed metal loadings of 4 mg cm⁻² on the anode and 2 mg cm⁻² on the cathode, the best performance is achieved when the metal loadings of the anode inner and outer catalyst layer and cathode inner and outer catalyst layer are set at 1.5, 2.5, 1.0, and 1.0 mg cm⁻², respectively.

Author Contributions: Conceptualization, Y.J.; Data curation, S.Z.; Formal analysis, S.Z.; Funding acquisition, S.Z.; Investigation, S.Z.; Methodology, S.Z.; Project administration, Y.J.; Resources, Y.J.; Software, S.Z.; Supervision, Y.J.; Validation, S.Z.; Visualization, S.Z.; Writing—original draft, S.Z.; Writing—review and editing, Y.J. All authors have read and agreed to the published version of the manuscript.

Funding: This research was funded by National Natural Science Foundation of China, grant number 62204100; China Postdoctoral Science Foundation, grant number 2021M691360; and Postdoctoral Research Foundation of Zhejiang Province, grant number ZJ2020101.

Data Availability Statement: Data is contained within the article.

Acknowledgments: Special thanks for the technical support from other researchers of the authors' group.

Conflicts of Interest: The authors declare no conflict of interest.

References

1. Li, Y.R.; Li, H.W.; Zhao, Y.; Ji, D.; Guo, P.; Li, G.X.; Zhao, X.H. Insights on the Roles of Nitrogen Configuration in Enhancing the Performance of Electrocatalytic Methanol Oxidation over Pt Nanoparticles. *Small* **2023**, *19*, e2303065. [[CrossRef](#)] [[PubMed](#)]
2. Zhao, M.L.; Xu, J.F.; Zhao, J.N.; Sun, S.S.; Tang, W.B.; Huang, Q.H.; Yu, N.F.; Wu, Y.P. Incorporation of ultralow manganese dioxide for improving the durability of sulfonated poly (ether ether ketone) membranes in passive direct methanol fuel cell. *Polymer* **2023**, *283*, 126204. [[CrossRef](#)]
3. Guo, S.Q.; Yu, S.Y.; Chen, F.; Wang, L.; Guo, M.; Ren, T.L.; Zhang, C.; Li, C.J. Direct methanol fuel cell with enhanced oxygen reduction performance enabled by CoFe alloys embedded into N-doped carbon nanofiber and bamboo-like carbon nanotube. *J. Colloid Interface Sci.* **2023**, *652*, 429–439. [[CrossRef](#)] [[PubMed](#)]
4. Jia, F.S.; Zhang, Y.J.; Zhang, P.; Zhang, X.T.; Hu, T.P. In situ growth of Ni/Ni₃S₂-MoO₂ nanocrystals on carbon cloth for the enhanced electrocatalytic oxidation of methanol. *Appl. Surf. Sci.* **2023**, *640*, 158348. [[CrossRef](#)]
5. Zuo, Y.H.; Sheng, W.C.; Tao, W.Q.; Li, Z. Direct methanol fuel cells system-A review of dual-role electrocatalysts for oxygen reduction and methanol oxidation. *J. Mater. Sci. Technol.* **2022**, *114*, 29–41. [[CrossRef](#)]
6. Bonham, D.; Choi, J.Y.; Kishimoto, T.; Ye, S.Y. Integrating PGM-Free Catalysts into Catalyst Layers and Proton Exchange Membrane Fuel Cell Devices. *Adv. Mater.* **2019**, *31*, e1804846. [[CrossRef](#)]
7. Yang, L.J.; Shui, J.L.; Du, L.; Shao, Y.Y.; Liu, J.; Dai, L.M.; Hu, Z. Carbon-Based Metal-Free ORR Electrocatalysts for Fuel Cells: Past, Present, and Future. *Adv. Mater.* **2019**, *31*, 1804799. [[CrossRef](#)]
8. Zhang, L.; Li, L.; Chen, H.M.; Wei, Z.D. Recent Progress in Precious Metal-Free Carbon-Based Materials towards the Oxygen Reduction Reaction: Activity, Stability, and Anti-Poisoning. *Chem. Eur. J.* **2020**, *26*, 3973–3990. [[CrossRef](#)]
9. de Sá, M.H.; Moreira, C.S.; Pinto, A.M.F.R.; Oliveira, V.B. Recent Advances in the Development of Nanocatalysts for Direct Methanol Fuel Cells. *Energies* **2022**, *15*, 6335. [[CrossRef](#)]
10. Kotp, A.A.; Abdelwahab, A.; Farghali, A.A.; El Roubi, W.M.A.; Allah, A.E. Evaluating the electrocatalytic activity of flower-like Co-MOF/CNT nanocomposites for methanol oxidation in basic electrolytes. *RSC Adv.* **2023**, *13*, 27934–27945. [[CrossRef](#)]
11. Lou, W.H.; Ali, A.; Shen, P.K. Recent development of Au arched Pt nanomaterials as promising electrocatalysts for methanol oxidation reaction. *Nano Res.* **2022**, *15*, 18–37. [[CrossRef](#)]
12. Reshetenko, T.V.; Kim, H.T.; Krewer, U.; Kweon, H.J. The effect of the anode loading and method of MEA fabrication on DMFC performance. *Fuel Cells* **2007**, *7*, 238–245. [[CrossRef](#)]
13. Reshetenko, T.V.; Kim, H.T.; Kweon, H.J. Cathode structure optimization for air-breathing DMFC by application of pore-forming agents. *J. Power Sources* **2007**, *171*, 433–440. [[CrossRef](#)]
14. Wang, G.X.; Sun, G.Q.; Wang, Q.; Wang, S.; Guo, J.S.; Gao, Y.; Xin, Q. Improving the DMFC performance with Ketien Black EC 300J as the additive in the cathode catalyst layer. *J. Power Sources* **2008**, *180*, 176–180. [[CrossRef](#)]
15. Wang, G.X.; Sun, G.Q.; Wang, Q.; Wang, S.L.; Sun, H.; Xin, Q. Effect of carbon black additive in Pt black cathode catalyst layer on direct methanol fuel cell performance. *Int. J. Hydrogen Energy* **2010**, *35*, 11245–11253. [[CrossRef](#)]
16. Roul, B.; Gorle, D.B.; Raj, G.; Kumar, K.; Kumari, M.; Nanda, K.K.; Krupanidhi, S.B. Solid-state synthesis of Pt/C cathode catalysts for direct methanol fuel cells. *J. Mater. Chem. C* **2023**, *11*, 11072–11081. [[CrossRef](#)]
17. Singh, H.; Zhuang, S.Q.; Ingis, B.; Nunna, B.B.; Lee, E.S. Carbon-based catalysts for oxygen reduction reaction: A review on degradation mechanisms. *Carbon* **2019**, *151*, 160–174. [[CrossRef](#)]
18. Kaur, A.; Kaur, G.; Singh, P.P.; Kaushal, S. Supported bimetallic nanoparticles as anode catalysts for direct methanol fuel cells: A review. *Int. J. Hydrogen Energy* **2021**, *46*, 15820–15849. [[CrossRef](#)]
19. Yuan, W.J.; Hou, C.J.; Wu, J.F.; Zhang, Y.F.; Zhang, X.L. A direct methanol fuel cell with outstanding performance via capillary distillation. *Chem. Eng. J.* **2023**, *470*, 143663. [[CrossRef](#)]
20. Alias, M.S.; Kamarudin, S.K.; Zainoodin, A.M.; Masdar, M.S. Active direct methanol fuel cell: An overview. *Int. J. Hydrogen Energy* **2020**, *45*, 19620–19641. [[CrossRef](#)]
21. Moura, A.S.; Fajin, J.L.C.; Mandado, M.; Cordeiro, M.N.D.S. Ruthenium-Platinum Catalysts and Direct Methanol Fuel Cells (DMFC): A Review of Theoretical and Experimental Breakthroughs. *Catalysts* **2017**, *7*, 47. [[CrossRef](#)]
22. Zhou, W.J.; Zhou, B.; Li, W.Z.; Zhou, Z.H.; Song, S.Q.; Sun, G.Q.; Xin, Q.; Douvartzides, S.; Goula, A.; Tsiakaras, P. Performance comparison of low-temperature direct alcohol fuel cells with different anode catalysts. *J. Power Sources* **2004**, *126*, 16–22. [[CrossRef](#)]
23. Tsai, M.C.; Yeh, T.K.; Chen, C.Y.; Tsai, C.H. A catalytic gas diffusion layer for improving the efficiency of a direct methanol fuel cell. *Electrochem. Commun.* **2007**, *9*, 2299–2303. [[CrossRef](#)]

24. Chang, Z.X.; Guan, L.; Zhang, J.J.; Zhang, W.Q.; Ma, Q.; Shah, A.; Xing, L.; Su, H.N.; Xu, Q. Construction of gradient catalyst layer anode by incorporating covalent organic framework to improve performance of direct methanol fuel cells. *Int. J. Hydrogen Energy* **2022**, *47*, 37013–37024. [[CrossRef](#)]
25. Li, X.; Yao, K.X.; Zhao, F.L.; Yang, X.T.; Li, J.W.; Li, Y.F.; Yuan, Q. Interface-rich Au-doped PdBi alloy nanochains as multifunctional oxygen reduction catalysts boost the power density and durability of a direct methanol fuel cell device. *Nano Res.* **2022**, *15*, 6036–6044. [[CrossRef](#)]
26. Wan, N.F. Durability study of direct methanol fuel cell under accelerated stress test. *J. Power Sources* **2023**, *556*, 232470. [[CrossRef](#)]
27. Tang, H.L.; Wang, S.L.; Pan, M.; Jiang, S.P.; Ruan, Y.Z. Performance of direct methanol fuel cells prepared by hot-pressed MEA and catalyst-coated membrane (CCM). *Electrochim. Acta* **2007**, *52*, 3714–3718. [[CrossRef](#)]
28. Xu, C.; Zhao, T.S.; Yang, W.W. Modeling of water transport through the membrane electrode assembly for direct methanol fuel cells. *J. Power Sources* **2008**, *178*, 291–308. [[CrossRef](#)]
29. Yang, W.W.; Zhao, T.S.; He, Y.L. Modelling of coupled electron and mass transport in anisotropic proton-exchange membrane fuel cell electrodes. *J. Power Sources* **2008**, *185*, 765–775. [[CrossRef](#)]
30. Yang, W.W.; Zhao, T.S. A transient two-phase mass transport model for liquid feed direct methanol fuel cells. *J. Power Sources* **2008**, *185*, 1131–1140. [[CrossRef](#)]
31. Zhou, J.; Cao, J.M.; Zhang, Y.F.; Liu, J.F.; Chen, J.Y.; Li, M.X.; Wang, W.Q.; Liu, X.W. Overcoming undesired fuel crossover: Goals of methanol-resistant modification of polymer electrolyte membranes. *Renew. Sustain. Energy Rev.* **2021**, *138*, 110660. [[CrossRef](#)]
32. Zhang, G.; Yang, Z.; Zhang, W.; Wang, Y.X. Nanosized Mo-doped CeO enhances the electrocatalytic properties of the Pt anode catalyst in direct methanol fuel cells. *J. Mater. Chem. A* **2017**, *5*, 1481–1487. [[CrossRef](#)]
33. Lu, G.B.; Ning, F.D.; Wei, J.; Li, Y.B.; Bai, C.; Shen, Y.B.; Li, Y.L.; Zhou, X.C. All-solid-state passive direct methanol fuel cells with great orientation stability and high energy density based on solid methanol fuels. *J. Power Sources* **2020**, *450*, 227669. [[CrossRef](#)]
34. Wu, H.J.; Yuan, T.; Huang, Q.H.; Zhang, H.F.; Zou, Z.Q.; Zheng, J.W.; Yang, H. Polypyrrole nanowire networks as anodic micro-porous layer for passive direct methanol fuel cells. *Electrochim. Acta* **2014**, *141*, 1–5. [[CrossRef](#)]

Disclaimer/Publisher’s Note: The statements, opinions and data contained in all publications are solely those of the individual author(s) and contributor(s) and not of MDPI and/or the editor(s). MDPI and/or the editor(s) disclaim responsibility for any injury to people or property resulting from any ideas, methods, instructions or products referred to in the content.